Self-Potential as a Tool to Monitor Redox Reactions at an Ore Body: A Sandbox Experiment

André Revil, Zhaoyang Su, Zhongmin Zhu, Alexis Maineult

minerals

MDPI

Article

Self-Potential as a Tool to Monitor Redox Reactions at an Ore Body: A Sandbox Experiment

André Revil [1], Zhaoyang Su [2,*], Zhongmin Zhu [3,4] and Alexis Maineult [5]

[1] Université Grenoble Alpes, University Savoie Mont-Blanc, CNRS, UMR CNRS 5204, EDYTEM, 73370 Le Bourget du Lac, France
[2] State Key Laboratory of Petroleum Resources and Prospecting, China University of Petroleum, Beijing 102249, China
[3] School of Civil Engineering, Shandong University, Jinan 250100, China
[4] Zhejiang Huadong Construction Engineering Co., Ltd., Hangzhou 310023, China
[5] Sorbonne Universités, CNRS, EPHE-UMR 7619 Metis, 4 Place Jussieu, 75005 Paris, France
* Correspondence: 2019310419@student.cup.edu.cn

Abstract: Ore bodies generate natural electrical fields that are measurable at the ground surface. The ground surface signature of this electrical field is called a self-potential anomaly. We developed a sandbox experiment to monitor the evolution of a self-potential anomaly associated with redox processes mediated by bacterial activity at the surface of a buried metallic object crossing the water table. A Bio-Electrochemical Cell (BEC) is formed by a metal bar connecting the upper, oxygen-rich, part of the tank and an aquifer containing an electron donor in the form of acetate. The self-potential response was observed during a period of 327 days. The tomography of the self-potential signature confirms that self-potential tomography is able to locate the metallic target acting as a BEC. In addition, we performed redox potential, pH, and electrical potential measurements over a vertical cross-section of the tank at several time steps to obtain an idea of where the redox front is located. The distributions of the redox potential and pH further demonstrated the development of the oxidation-reduction chemical processes facilitated by the BEC as bacterial communities developed around the metallic bar. The electrical potential anomaly shows that the bacterial communities followed a short period of exponential growth, then a longer period of a sustained population. These results demonstrate the usefulness of the self-potential method in monitoring redox processes at the surface of a buried ore body. Further works will need to combine such self-potential anomalies with induced polarization anomalies through joint inversion.

Keywords: self-potential; redox reactions; ore body; monitoring; tomography; bioleaching

Citation: Revil, A.; Su, Z.; Zhu, Z.; Maineult, A. Self-Potential as a Tool to Monitor Redox Reactions at an Ore Body: A Sandbox Experiment. *Minerals* **2023**, *13*, 716. https://doi.org/10.3390/min13060716

Academic Editor: Behnam Sadeghi

Received: 23 March 2023
Revised: 16 May 2023
Accepted: 16 May 2023
Published: 24 May 2023

1. Introduction

Previous studies have examined the existence of geobatteries and biogeobatteries associated with ore bodies and buried metallic objects in the subsurface of the Earth (e.g., [1–7]). Revil et al. (2015) [8] created a BioElectrochemical Cell (BEC) in a simulated groundwater environment. They demonstrated that the introduction of an organic contaminant (propylene glycol in their case) around a buried metallic object can serve as an electron donor with bacteria playing the role of catalysts at the ore surface. In marine investigations of ore bodies, it is known that self-potential anomalies can be recorded near the sea floor associated with sulfide deposits [9,10]. Self-potential tomography and source localization techniques has been demonstrated to be a powerful method to localize these ore bodies [11–21]. However, none of the previous studies considered examining the geo-electrical response of a BEC with an organic contaminant for a long period of time. Dynamic experiments in which redox conditions are modified at the surface of the ore body and the resulting self-potential field monitored have never been performed to date.

Another area of interest is bioleaching. Bioleaching is used to extracts metals from ore bodies using ferrous iron and sulfur oxidizing bacteria, or, in some cases, fungi [22,23]. Since bacteria may play the role of catalysts, they lower potential barriers for electron transfer at the surface of the ore. The kinetics of redox reactions at the surface of an ore body could be therefore monitored using time-lapse self-potential signals.

Our goal in this paper is to demonstrate that the self-potential method can be used to monitor redox processes at the surface of an ore body. We perform a long-term sandbox experiment (for 337 days) in which a buried metallic bar is used as a proxy of an ore body. The goal of the experiment is to monitor the self-potential field by creating various perturbations in the sandbox that may affect the redox reactions at the surface of the metallic object and to look at the changes in the resulting self-potential field associated with the BEC. We also demonstrate that self-potential tomography can be used to monitor the volumetric current source density at the position of the metallic target.

2. Experimental Setup and Results

2.1. Sandbox Experiment

Figure 1 shows the experimental setup used in this study. For this experiment, we used an insulating glass tank with inner dimensions of x = 89 cm and y = 45 cm and outer dimensions of x = 90 cm and y = 45 cm. We selected a uniform quartz sand with a mean grain size of d_{50} = 0.35 mm (Unimin Corporation 4060) and a porosity of 0.503. The tank was filled to a height of 32 cm from the bottom of the tank with the sand, with special care taken to ensure a homogeneous distribution of the sand (Figure 1). We added water concurrently with the sand during construction in order to drive pockets of air out of the pore space and create a truly saturated subsurface to an initial height of 17 cm above the bottom of the tank. The capillary fringe was then allowed to develop through capillary suction within the pore space of the sand immediately above the phreatic surface. A plastic pipe of dimensions 4 cm in diameter and 35 cm in length was placed at the location (x = 2 cm, y = 2 cm) in the tank, which allowed us to add water to the tank environment during the initialization and experimentation phases to offset evaporation. The pore water conductivity was ~0.042 S m^{-1} (tap water, 25 °C) and the temperature of the experiment was maintained at 23 ± 2 °C.

To simulate a BEC, an industry standard object (ISO) munitions analog (part number 44615K466 of the McMaster-Carr catalog, USA) was added to the center of the tank as described in [3] (Figure 1c). The ISO we chose is a hollow stainless-steel cylinder with dimensions of 33 mm outer diameter, 30 mm inner diameter, and 101 mm length, which we will refer to as the metal body/target below. On the outside of this metal body was a protective coating (blackened steel) originally applied by the manufacturer to prevent the metal body from corroding during industrial use. To allow corrosion to occur, this protective coating was removed (on both sides) prior to burial through the use of abrasives. The metal body was then placed vertically in the center of the tank at location x = 45 cm, y = 22.5 cm, and z = 19 cm. The top of the metallic bar was located 8 cm below the surface of the sand. Sand was then introduced around the metal body once in place, including within its hollow interior. Once buried, the metal body remained undisturbed during the whole experiment.

2.2. Measurements

During the experiment, we altered the chemical conditions of the tank by inducing two changes in the level of the phreatic surface. The first change (Day 1) modifies the water table from z = 17 cm (middle of the metallic target) to z = 10.5 cm—below the metallic target (see Figure 1). The second change (Day 61) was performed in order to modify the height of the water table from z = 10.5 cm (water table below the metallic target) to z = 17 cm (water table at the center of the metallic target). The two changes occurred 22 days apart (Figure 2). The two perturbations in the phreatic surface served to diminish a pre-existing

self-potential signal that developed within the tank during the initialization phase and re-established the original conditions of the tank, respectively, at a later date (Day 22).

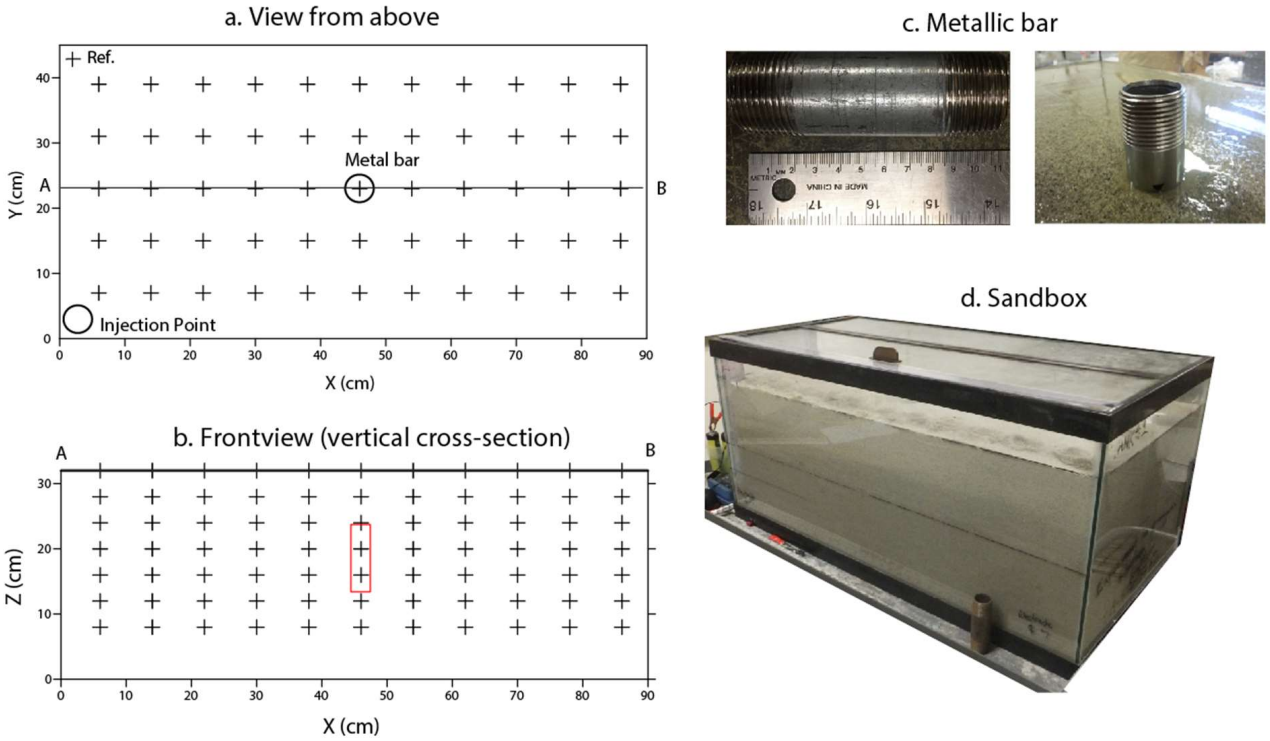

Figure 1. Experimental setup. (**a**) Diagram showing the positions of the 2D-self-potential measurements (crosses) in mapview, with the positions of the metal bar, the reference electrode, and the fluid injection pipe described. "Ref" denotes the reference electrode for the electrical potential measurements. The crosses refer to the measurement stations. (**b**) Diagram showing the placement of measurements along 2 vertical cross-sections (self-potential, pH, and Eh) from the front (x/z) view. The metal bar is outlined in red and the reference position for vertical self-potential is included in the top left of the plot. The crosses refer to the measurement stations. (**c**) The metal bar used in this experiment: a hollow stainless-steel bar with oxidation coating removed. The second picture shows the metal bar submerged in the tank environment during tank construction. (**d**) Photograph showing the constructed tank during experimentation.

Two additions of acetic acid injected through the borehole are shown in Figure 1 approximately 15 days apart. The introductions of acetic acid into the tank then encouraged the development of a BEC by allowing the acetic acid to dissociate into acetate and hydrogen ions. Aerobic bacteria could then metabolize the acetate and begin to flourish. Because oxygen is a limiting factor in the capillary fringe and below the water table where the bacteria are most present, the conductive pathway of the metallic bar allowed a conduit for electrons to travel and reduce free oxygen in the upper part of the capillary fringe, thus completing the oxidation-reduction coupling of the BEC.

Two-dimensional self-potential measurements were collected at the top surface of the tank along a grid emplaced in the sand prior to measurement collection (Figure 1a,b). The measurement grid was embedded into the surface of the tank using a plexiglass frame prepared according to [3]. This grid contained a total of 55 stations (x = 11 stations and y = 5 stations) placed 7.8 cm apart in both x- and y-directions. The hole closest to the origin was placed at coordinates x = 8 cm and y = 7 cm, which each of the other stations followed in a regular 11 × 5 grid, as described above. The reference electrode was placed at coordinates x = 3 cm and y = 40 cm. No measurement of the electric potential difference was collected at the position immediately below the reference electrode, and the reference electrode

was not placed as part of the measurement grid. The electrodes used for the 2D-self-potential measurements were copper–copper sulfate ($Cu/CuSO_4$) electrodes manufactured by Tinker & Rasor (New Braunfels, TX, USA). The diameter of the electrodes is 2 cm and they were pushed into the sand at a depth of roughly 1 mm. Measurements were taken on a MX55 Multimeter manufactured by AEMC Instruments with an internal impedance of 10 MOhm. The resulting self-potential anomalies are shown 8 times in Figure 3.

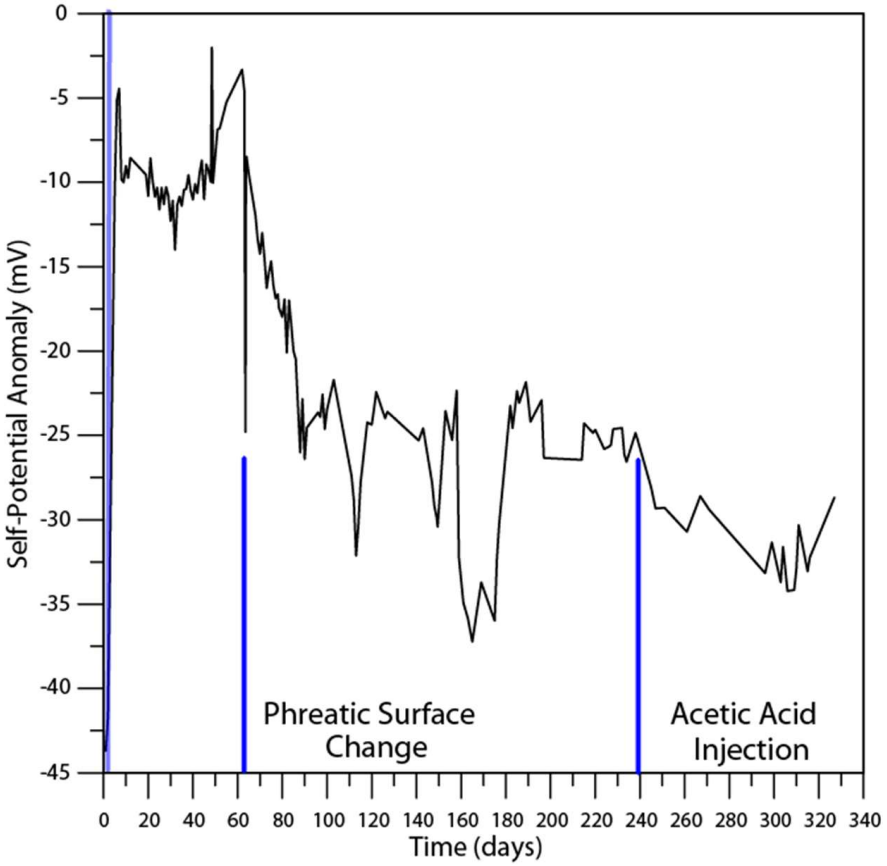

Figure 2. Development of the peak of the self-potential anomaly above the metallic bar and over the course of the experiment. The self-potential response chosen for this graph represents Station 28 (x = 45 cm, y = 22.5 cm), which is the position immediately above the metallic bar. Larger negative values indicate stronger responses. The blue lines indicate the days where the height of the phreatic surface was altered and intersect the associated self-potential response.

All vertical measurements (including vertical self-potential data, redox potential, and pH data) were performed in two vertical planes bisecting both the x- and y-directions of the tank at the position of the metallic bar. At each station, we performed a set of measurements beginning at the surface (z = 32 cm) and continuing downward to z = 8 cm in 4 cm increments for a total of 117 measurements for both lines (Figure 1a,b). For self-potential measurements along vertical cross-sections, the reference electrode was placed in the same location as in the 2D-self-potential survey at the top surface. The electrodes used in this survey were two micro pellet sintered $Ag/AgCl_2$ non-polarizing electrodes provided by Science Products Gmbh (Hofheim am Taunus, Germany) with dimensions of 2 mm in diameter and 2 mm in length. All pH measurements were conducted with a pH Combination Electrode PY-P11 from Sartorius, Bohemia, NY, USA with an integrated temperature sensor. All redox potential measurements used an InLab Orion^{TM}REDOX-ORP Redox Probe (Fischer Catalog, Racine, WI, USA) with the platinum ring indicator. Both the pH and Eh probes connect to an UP-25 handheld pH/ion/mV meter manufactured by Denver Instruments in Bohemia, NY, USA.

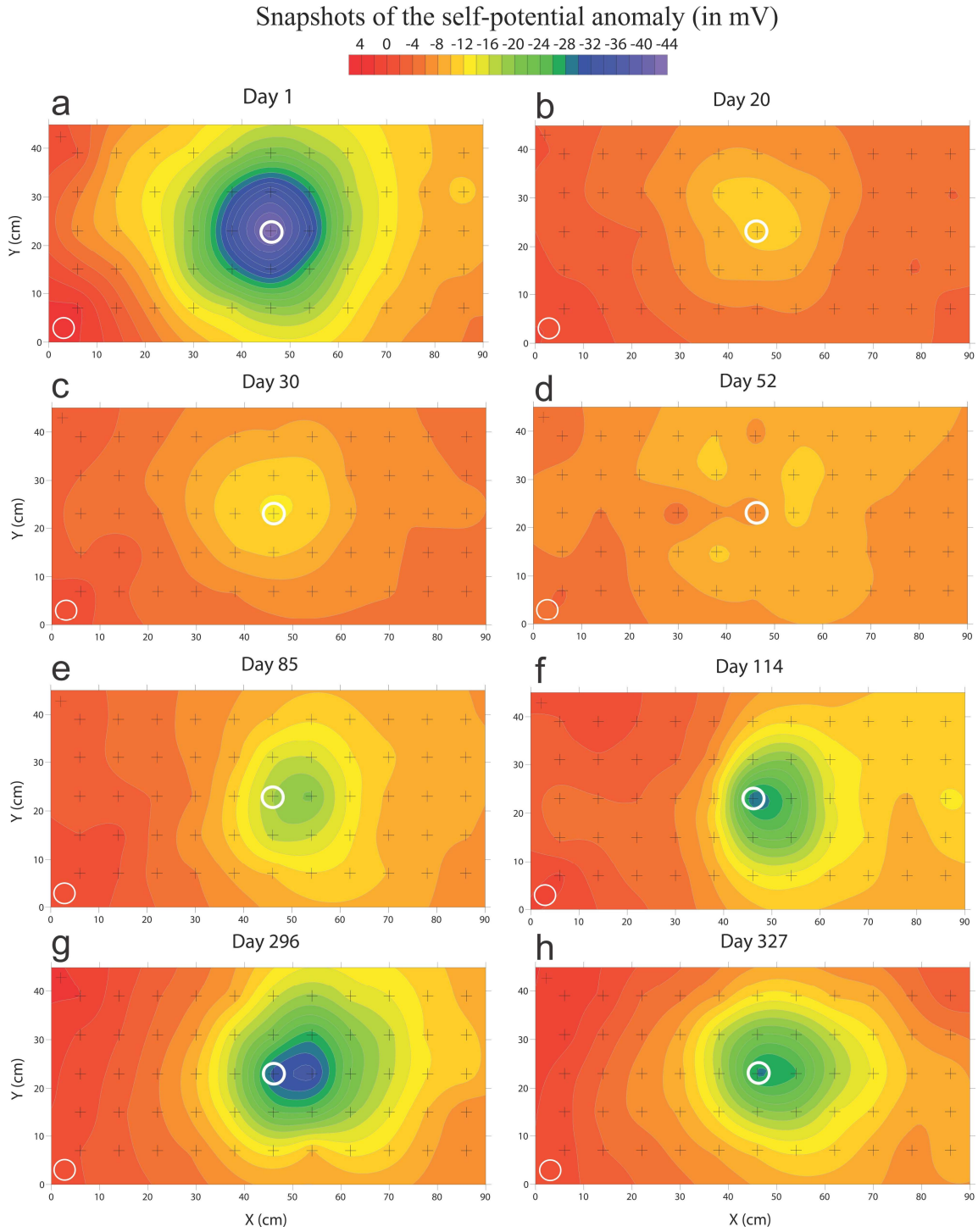

Figure 3. Development of the self-potential anomaly over time. (**a**) Initial conditions and the beginning of Phase 1 (with a maximum anomaly of −44 mV). (**b**) During Phase 1, shortly after the first perturbation of the phreatic surface. (**c**) During Phase 2. No anomaly. (**d**) During Phase 3, after the first injection of acetic acid. (**e**) During Phase 4, after the second injection of acetic acid where the phreatic surface changed rapidly. (**f**) During Phase 5, after the 2D-self-potential anomaly had stabilized. (**g**) At the end of Phase 5, the 2D-self-potential anomaly reaches its maximum amplitude. (**h**) Self-potential distribution at the conclusion of the experiment (end of Phase 5). The white circle in the center of the map corresponds to the projection of the metallic bar.

In 2016, we performed a second experiment for a month similar to the experiments used for the self-potential measurements. After one month, samples were removed from the tank for the purposes of extracting bacteria and fluid-laden sediment for DNA/RNA sampling. The purpose of this was to determine which varieties of bacteria had metabolized within the tank. To do this, three cores were chosen to be representative of the tank environment.

2.3. Description of the Experiment

The experiment was carried out over the course of approximately 18 months as one continuous experiment, beginning with the construction of the tank in December 2013 and concluding with final sampling of the tank in April 2015. The progress of the experiment can be considered as two separate phases: the initialization phase from December 2013 to June 2014 and the experimentation phase itself, taking place from June 2014 to April 2015. Only the experimental phase will be considered in this paper (starting at Day 1). Both phases used the same experimental setup.

Over the course of experimentation, a total of 152 sets of 2D-self-potential measurements were recorded. In the early time steps of the experimentation phase (Day 1 through Day 120), 2D-self-potential measurements were recorded approximately once every 24 h. It was during this part of the experiment that all of the perturbations to the tank environment were conducted, including both of the changes to the height of the phreatic surface and both injections of acetic acid. It was also during this period that we saw the greatest change in the self-potential signals over time. As the experiment progressed, the interval between 2D-self-potential measurements was relaxed to intervals of 24–72 h, which was allowed as the signal stabilized.

At the beginning of the experimentation phase, the tank environment was composed of the metallic bar at the center of the tank (x = 45 cm, y = 22.5 cm, z = 19 cm) that had begun to corrode, producing a strong self-potential signal (Figure 3). We dropped the height of the phreatic surface from its initial height of z = 17 cm to a maintained height of z = 10.5 cm during the course of the initialization phase (Day 1 to Day 22). The phreatic surface and its associated capillary fringe were uniformly distributed throughout the tank. At this stage, the subsurface of the tank had not been perturbed in any significant way following the initial construction of the tank. No sharp perturbations to the water table had occurred and no organic contaminants, specifically the acetic acid solution used in this experiment, had been introduced into the subsurface.

Given the perturbations to the tank we intentionally caused, as well as the resulting self-potential signal that formed, we can divide the experimentation phase into 6 main phases, labeled below: Phase 1 to 6.

Phase 1 (21 days): The period beginning at the start of the experimentation phase (Day 1) and ending at the second perturbation of the phreatic surface (Day 22). The water table was lowered and then raised to decrease the magnitude of the self-potential signal, as shown in Figures 2 and 4. At the beginning of Phase 1, we observed a strong 2D-self-potential anomaly with a magnitude of −43 mV at the center position, which marked the largest magnitude recorded during the whole experiment. We considered this measurement to be our initial conditions, as the anomaly developed under conditions that were consistent with those demonstrated in [3]. Upon raising the phreatic surface from z = 10.5 cm to z = 17 cm on Day 2, the magnitude of the anomaly quickly dropped in magnitude to approximately −5 mV with little discernible anomalies visible in the 2D-self-potential measurement.

Phase 2 (24 days): The period from the second perturbation of the phreatic surface (Day 22) to the first injection of acetic acid (Day 48). During this phase, the water table is at the level of the metallic target and the self-potential anomaly remains weak, at around −10 mV.

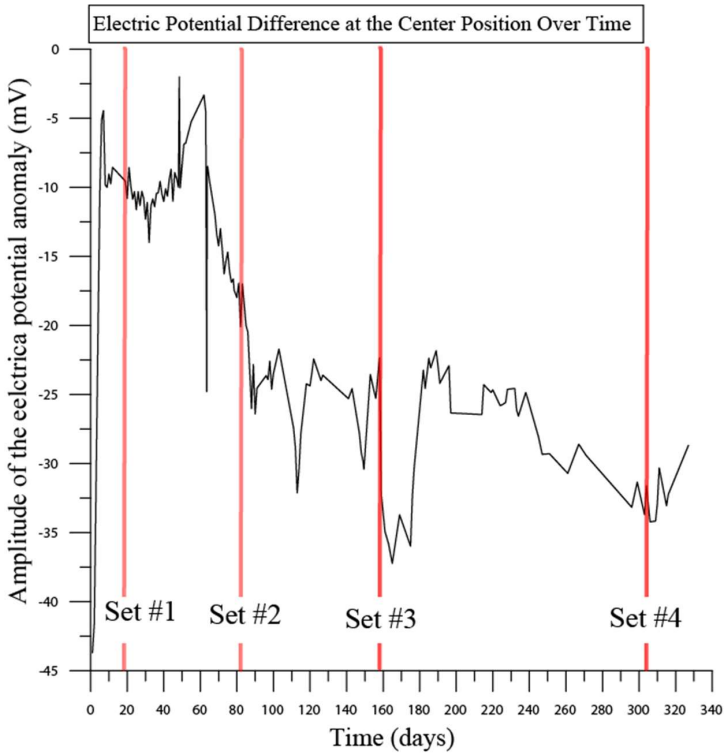

Figure 4. Development of the self-potential anomaly above Station 28 (the center point). Larger negative values indicate stronger source current density at the metallic target. The red lines indicate the time steps where a set of measurements along two vertical cross-sections were performed (Day 19, Day 81, Day 158, and Day 303).

Phase 3 (15 days): The period between the first (Day 48, 40 mL injected) and second injections of acetic acid (Day 63, 40 mL injected). The first injection of acetic acid does not modify the amplitude of the self-potential anomaly much, likely because it takes a lot of time to reach the homogenization of the acidic pore water in the tank.

Phase 4 (51 days): The period between the second injection of acetic acid (Day 63, 40 mL) and the stabilization of the self-potential anomaly around −25 mV (Day 113). The second injection of 40 mL of acetic acid was applied at the beginning of Phase 4 directly at the top of the metallic body, which produced a sharp initial perturbation of −20 mV on the day of the application and later initiated a gradual increase in the 2D-self-potential anomaly at the center location.

Phase 5 (215 days): The period between the stabilization of the signal and the reinitiation of development near the end of the experiment (Day 114 to Day 327). By the beginning of Phase 5, the growth of the anomaly ceased at approximately −30 mV at the center point, and then stabilized at approximately −25 mV until Day 239. However, a set of measurements along a vertical cross-section on Day 159 appeared to perturb the tank and create a response of −32 mV that persisted for 18 days before returning to the original potential difference. Then, the magnitude of the anomaly gradually increased again to an average magnitude of −33 mV, which persisted for a long time, nearly to the end of the experiment. By the end of experimentation, the anomaly had begun to decrease in magnitude at the center position, ending with a potential difference of −28 mV.

Unlike the 2D-self-potential measurements, the measurements along the vertical cross-sections (self-potential, redox potential, and pH) were performed at 4 specific dates during experimentation (Day 19, Day 81, Day 158, and Day 303). Each set of measurements took place over the course of 3–5 days and were always accompanied by 2D-self-potential measurements taken immediately before any vertical measurements conducted on any given day. All measurements along the two vertical cross-sections conducted at a particular timestep were obtained concurrently. Measurement sets were chosen to coincide with

four critical stages of the experiment: Measurement Set #1: before the injection of acetic acid (Phase 1); Measurement Set #2: during the period of exponential growth of the 2D-self-potential signal and following the injection of acetic acid (Phase 4); Measurement Set #3: during the stable phase following the exponential growth of the 2D-self-potential signal (Phase 5); and Measurement Set #5: at the conclusion of the experiment (Figure 4).

As mentioned above, a replica of the experiment was conducted for one month to be able to sample the sand and the surface of the metallic object for DNA/RNA sequence analysis in order to have an idea of the bacterial populations that are present during the experiment, using polymerase chain reaction (PCR) and sequencing technologies [23–25].

3. Interpretation

3.1. Forward Analysis of the Self-Potential Signals

Figure 3 shows the change in the corrected measured value of the 2D-self-potential anomaly over the course of the experiment. Specifically, each point on the graph represents the value of Station 28 (x = 45 cm, y = 22.5 cm), relative to a reference potential at 0 mV. This station was chosen because it corresponds to the position immediately above the metallic bar and will be referred to as the 'center position' throughout the report (x = 45 cm, y = 22.5 cm). Relative to the reference potential, the electrical potential anomaly measured for all time steps was negative and therefore the associated source current density within the tank is oriented vertically downward. All 2D-self-potential data sets are plotted on the same color scale to aid in a direct comparison (Figure 3). Figure 2 shows the 2D-self-potential responses at each phase of the experiment, as well as the responses recorded at the beginning and conclusion of experimentation.

The self-potential problem can be written through the use of a constitutive and a charge conservation equation written in the quasi-static limit of the Maxwell equations as

$$\mathbf{j} = \sigma\mathbf{E} + \mathbf{j}_S, \tag{1}$$

$$\nabla\cdot\mathbf{j} = 0. \tag{2}$$

In these equations, $\mathbf{j}$ denotes the total current density; σ denotes the DC (Direct Current) conductivity; $\mathbf{j}_S$ the source current density associated with redox processes, which can be mediated by bacteria acting as catalysts. The electrical fields are related to the electrical potential by $\mathbf{E} = -\nabla\varphi$. The electrical potential therefore obeys an elliptic equation given by [26],

$$\nabla^2\varphi + \nabla \ln\sigma\cdot\nabla\varphi = \frac{\nabla\cdot\mathbf{j}_S}{\sigma}, \tag{3}$$

Forward modeling consists in choosing a distribution of the electrical conductivity and a distribution of source current density, as well as solving the previous partial differential equation to compute the self-potential distribution everywhere in the domain of interest, including at the ground surface.

In order to estimate the distribution of the electrical potential along the metallic cylinder, we applied the methodology developed by Maineult in 2016 [7]. We note the electrical potential distribution along the buried metallic object S(d), below where d is the depth. We also know the electrical conductivity distribution in the whole tank. Then, Poisson equation can be solved in cylindrical coordinates to compute the associated distribution of self-potential (denoted $\psi(r,d)$, where r is the radial distance) inside the whole medium (and therefore the SP profile $\psi_s(r)$ at the surface of the metallic object). Using the finite difference scheme, the problem is linear and $\mathbf{V} = \mathbf{M}^{-1}\,\mathbf{S}$, where $\mathbf{M}$ denotes a square sparse matrix. Here, we know $\psi_s(r)$ and we search for S(d), which is defined by a spline (with four nodes here) using an optimization procedure based on the simulated annealing (such as in Maineult 2016 [7], but without the monotony constrain on $\psi_s(r)$). Note that we modified the original code to have insulating conditions (i.e., Neumann condition) at a depth of d = 32 cm, and at a radial distance of r = 44.5 cm to mimic the sandbox conditions.

The limitation of this approach is that we consider a finite cylindrical medium, instead of a rectangular box. The surface SP profiles $\psi_s(r)$ are extracted from the self-potential surface measurements (Figure 3) by taking the SP values at the coordinates y = 23 cm, and x = 46, 54, 62, 70, 78, and 86 cm (dots in Figure 5b). For the electrical conductivity of the saturated zone, we apply the simplest Archie first formula, using a cementation exponent of 2. Using a water conductivity of 0.042 S m^{-1} and a porosity of 0.503, the conductivity of the saturated zone is equal to 0.01 S m^{-1}. For the conductivity of the unsaturated zone, we divided this value by 5 and consider it as homogeneous in a first approximation (we neglect the capillary fringe). The deduced electrical distributions S(d) are represented in Figure 5a, and the computed SP profiles are represented as a continuous line in Figure 5b. The predicted values are in good agreement with the data. Concerning the electrical potential distributions along the cylinder, they are dipolar in nature, with negative values for smallest depths and positive values for larger depths. This is coherent with the results obtained by Maineult (2016) [7] for a metallic casing, and with the results obtained by Rittgers et al. (2013) [3] during the corrosion of a metallic body in a sandbox. The amplitude of the dipole decreases with time from Day 1 (where there is an already a strong signal) to Day 30. Then after the first injection of acetic acid, the amplitude of the dipole increases again (Day 52), and again after the second injection (Day 85). During Phase 5, the amplitudes continues to increase (Day 296), meaning that some processes still enhance the corrosion.

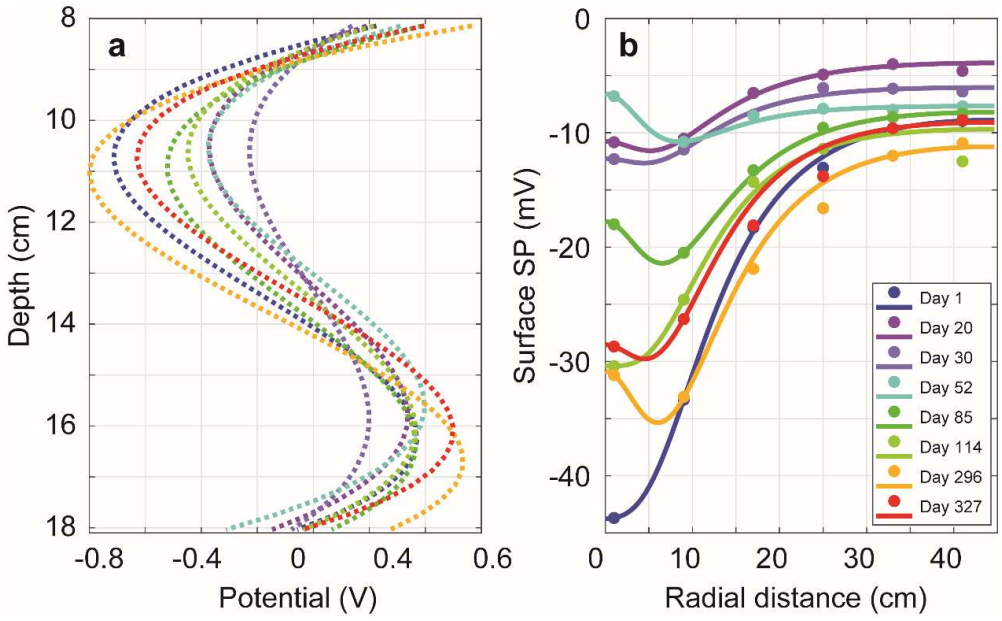

Figure 5. Dipolar nature of the current source at the surface of the metallic object. (**a**) Electrical potential distribution along the surface of the metallic object. (**b**) Fit of the self-potential profiles at the top surface of the tank used as inputs. The plain lines correspond to the best fit of the measured self-potentials for the eight snapshots used in the analysis.

3.2. Self-Potential Tomography

Self-potential tomography consists in retrieving information regarding the causative source of the current responsible for the self-potential anomaly recorded at the ground surface, here measured at the top surface of the tank at a set of discrete locations shown in Figure 1a. The general objective function in the self-potential inversion is defined as [27]

$$\phi(\mathbf{m}) = \left\|\mathbf{W}_d(\mathbf{d}_{\text{obs}} - \mathbf{d}_{\text{pre}})\right\|_2^2 + \beta\left\|\mathbf{W}_m(\mathbf{m} - \mathbf{m}_{\text{ref}})\right\|_2^2 \quad (4)$$

where the β denotes the regularization parameter that balances the data misfit term and model constrain term. The cooling strategy is used to select an appropriate value β; $\mathbf{W}_d$ is

a diagonal data-weighting matrix; $\mathbf{d}_{\text{obs}}$ and $\mathbf{d}_{\text{pre}}$ denote the observed and predicted data, respectively; $\mathbf{W}_m$ denotes the roughness operator used to obtain a smooth model $\mathbf{m}$; and $\mathbf{m}_{\text{ref}}$ denotes the reference model. The first term of the right-hand side of Equation (4) denotes the data misfit term while the second term is the regularization function.

Here, we use the minimum support (MS) method to recover a compact volumetric source current density. The MS function is defined as [28]

$$\text{MS} = \sum_{i=1}^{M} \frac{m_i^2}{m_{i(k-1)}^2 + \beta^2} \tag{5}$$

where M denotes the number of cells, $\text{m}_{i(k-1)}$ is the inverted model at the iteration (k–1), and β is a small threshold value (see [28]). A depth-weighting matrix is applied to the kernel in order to recover a realistic and meaningful source model [29]. The weighting matrix is defined as

$$\mathbf{\Lambda} = \text{diag}\left(\sum_{i=1}^{N} K_{ij}^2\right)^{1/4} \tag{6}$$

With the MS function, a new diagonal matrix is

$$\mathbf{\Pi} = \text{diag}\left(\sqrt{\frac{\Lambda_{kk}^2}{m_{k-1}^2 + \beta^2}}\right) \tag{7}$$

Thus, Equation (4) can be rewritten as

$$\phi(\mathbf{m}_w) = \|\mathbf{W}_d(\mathbf{K}_w\mathbf{m}_w - \mathbf{d}_{\text{obs}})\|_2^2 + \beta\|\mathbf{W}_m(\mathbf{m}_w - \mathbf{m}_{\text{ref}})\|_2^2 \tag{8}$$

where the new kernel matrix is $\mathbf{K}_w = \mathbf{K}\mathbf{\Pi}^{-1}$, Equation (8) is linear with respect to $\mathbf{m}$ and can be easily minimized. The following solution for the model vector is obtained by setting the derivative of the cost function, Equation (8), with respect to the model vector; we obtain,

$$\mathbf{m}_w = [\mathbf{K}_w^T(\mathbf{W}_d^T\mathbf{W}_d)\mathbf{K}_w + \beta(\mathbf{W}_m^T\mathbf{W}_m)]^{-1} \cdot [\mathbf{K}_w^T(\mathbf{W}_d^T\mathbf{W}_d) + \beta(\mathbf{W}_m^T\mathbf{W}_m)\mathbf{m}_{\text{ref}}] \tag{9}$$

The distance-corrected model can be retrieved using the following transform $\mathbf{m} = \mathbf{\Pi}^{-1}\mathbf{m}_w$ after the final iteration in order to properly reweight the solution [30,31]. The self-potential inversion starts with a uniform model (no prior) and a 3D uniform conductivity distribution (a constant value of 0.01 S m^{-1}, [3]). The convergence condition is that the mean square error between the observed data and predicted data convergences to the root-mean-square (RMS) error of 1.0 or reaches to a maximus number of iterations (the maximum number we set is 10), and the RMS is defined as

$$RMS = \sqrt{\frac{\phi_d(\mathbf{m})}{N}} \tag{10}$$

where N denotes the number of observed data. $\phi_d(\mathbf{m})$ (the first term on the right-hand side of Equation (8)) denotes the data misfit in the objective function. After several iterations, the inversion results are shown in Figure 6. Each column of the Figure 6, from left to right, presents the recovered 3D (volumetric) source current density distribution, the inferred metal bar from inverted data (gray domain where the magnitude of current density is larger than 1 mA m^{-3}). Same as the observed self-potential data in Figure 6, the highest magnitude of the 2D-self-potential anomaly is at the beginning of Phase 1; thus, the inverted source current density agrees with the position of the metal bar. Then, the change of the phreatic surface during the Phase 2 delays the redox reaction, and the 2D-self-potential anomaly did not occur; thus, the invert result cannot be used to infer the position of the metal bar. The two injections of acetic acid solution make corrosion processes recommence, then the growth of the 2D-self-potential anomaly reached its maximum in Phase 5, and the

inferred position of metal bar is the best. Figures 7 and 8 show the cross-section and allow a comparison between the distribution of the inferred volumetric current source and the true position of the metallic bar.

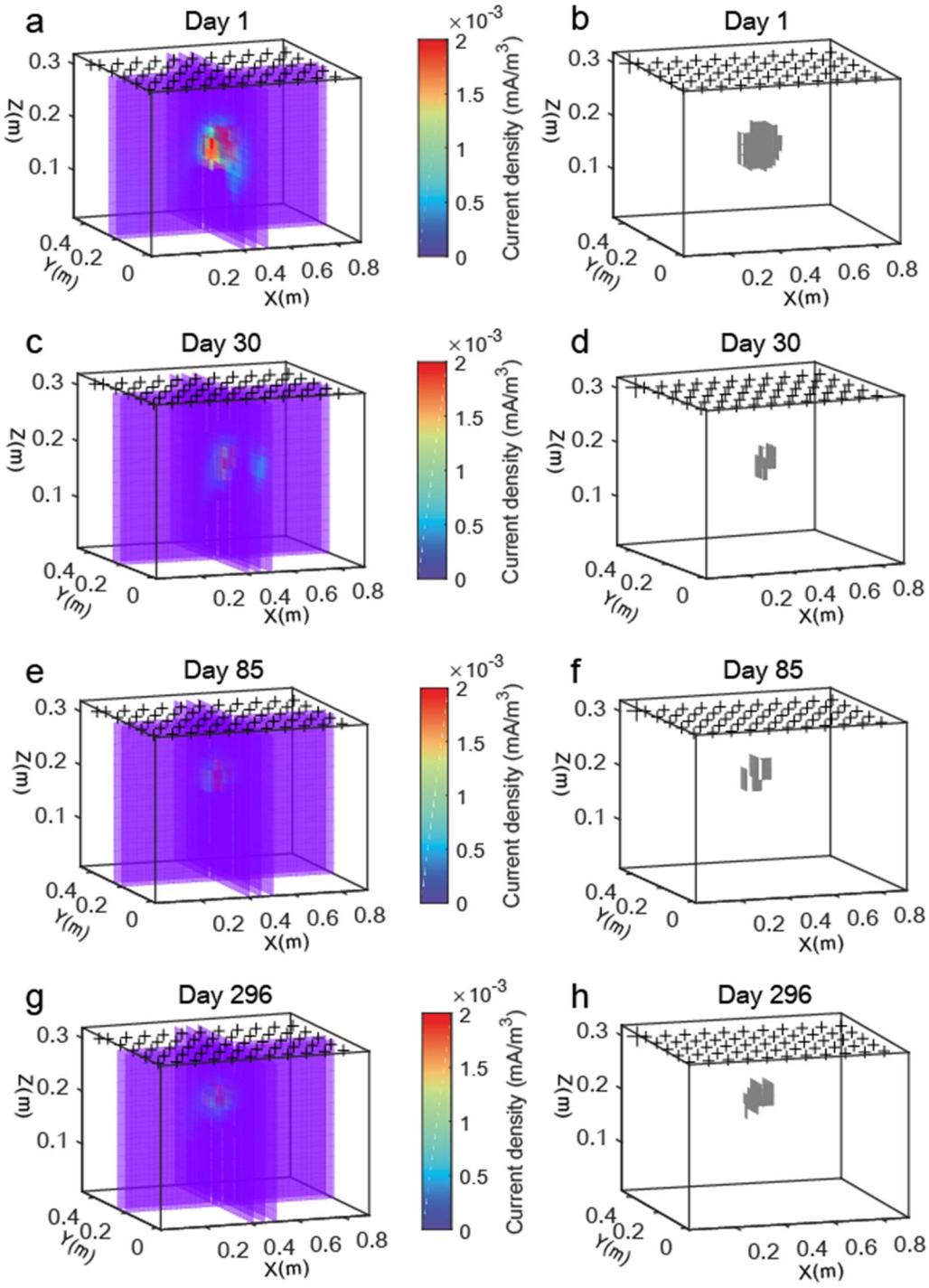

Figure 6. Self-potential tomograms at 4 selected times using the surface self-potential data measured at a set of discrete locations shown in Figure 1a. (**a**,**b**) The 3D current density distribution at the beginning of Phase 1 (Day 1). (**c**,**d**) The 3D current density distribution during the Phase 2. (**d**) Result at Day 30 with a small self-potential anomaly (see Figure 3). (**e**,**f**) The 3D current density distribution after the injection of acetic acid during Phase 4. (**g**,**h**) The 3D current density distribution during Phase 6.

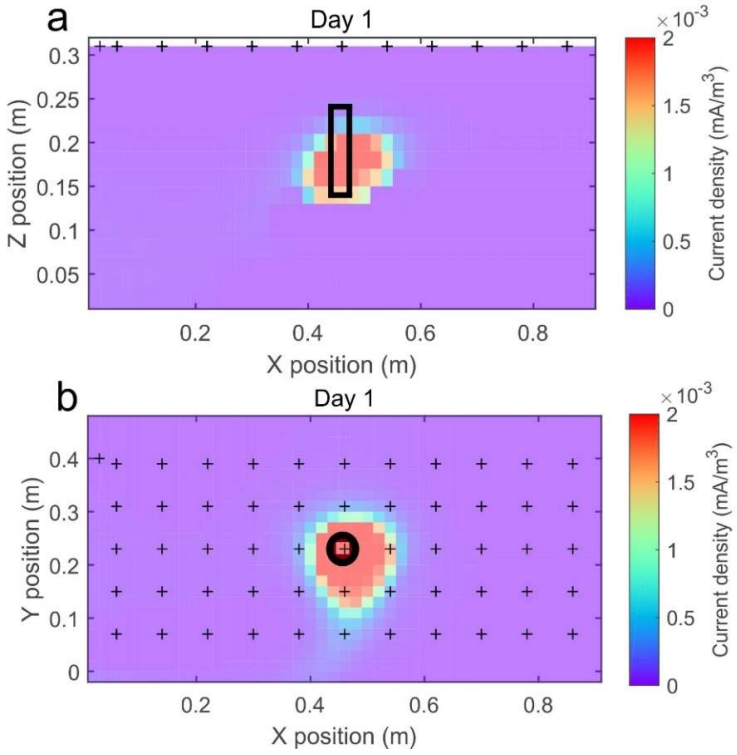

Figure 7. Inverted 3D volumetric current source density distribution at the beginning of Phase 1 (Day 1). The black solid line underlines the true position of the metal bar. (**a**) The 2D vertical cross section's current density distribution from the front (x/z). (**b**) The 2D horizontal cross section's current density distribution from the front (x/y).

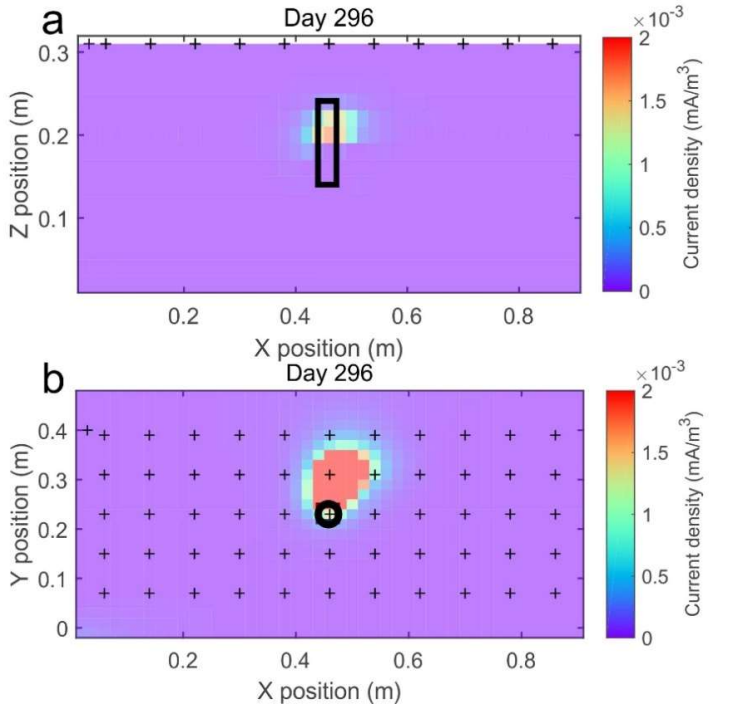

Figure 8. The inverted 3D current density distribution at Day 296 and the positions of the metal bar. (**a**) The 2D vertical cross section's current density distribution from the front (x/z). (**b**) The 2D horizontal cross section's current density distribution from the front (x/y). The thick black lines underline the position of the metallic object.

We have a good agreement between the two that will be further discussed below. Figure 9 shows that the observed data (Day 296) is well reproduced by the inverted volumetric current source. This indicates that self-potential tomography is effective in localizing metallic ores.

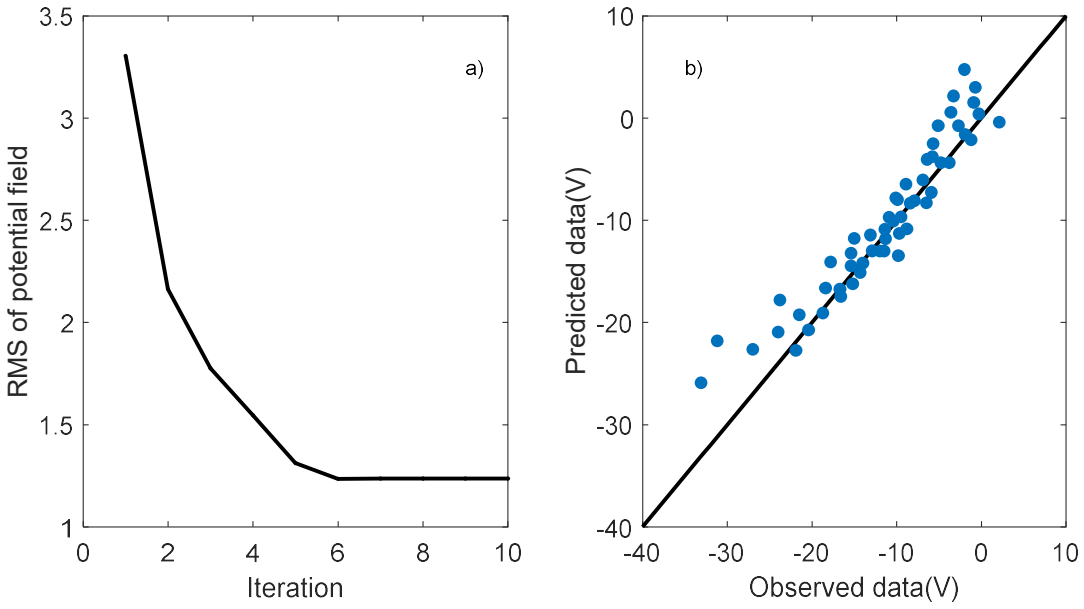

Figure 9. Convergence of the self-potential inversion and fit between the observed and predicted data. (**a**) Root-mean-square (RMS) of the self-potential data misfit (for the observed electrical field with 5% noise) as a function of the number of iterations used to minimize the objective function. (**b**) Observed data versus the predicted data for the last iteration. We observe that the recoded data are well-reproduced by the inverted model.

3.3. Analysis of the 3D Data Sets

Concerning the 3D data sets, four sets were obtained during the course of the experiment (Figure 4). Data Set #1 was conducted on Days 19–21 to coincide with Phase 1 and included only redox potential data. Data Set #2 was conducted on Days 83–85 to coincide with Phase 4 and consisted of 3D-self-potential and redox potential data. Measurement Set #3 was conducted on Days 158–159 to coincide with Phase 5. It consisted of 3D-self-potential, pH, and redox potential data.

Measurement Set #1 observed a large negative redox potential anomaly at the bottom of the metal bar of −380 mV, the largest observed during experimentation (Figure 10). This indicated that redox conditions still existed despite a lack of signal in the associated 2D-self-potential data, which remained around −8 mV to −10 mV throughout Phase 1. The redox potential dropped, however, between the front view data, which was collected first, and the sideview data, which was collected second, potentially indicating that measuring the redox potential in the face view disrupted the environment enough to be reflected in the sideview data collected shortly thereafter.

Measurement Set #2 observed a clear negative 3D-self-potential anomaly of −55 mV at the position of the top of the metal bar (Figure 11). The redox potential data also revealed a large negative redox potential anomaly of −130 mV at the bottom of the metallic bar, though it was much smaller in magnitude than that observed in Measurement Set #1, possibly due to the change of the redox gradient that came with lowering the phreatic surface at the end of Phase 1. These measurements did not seem to affect the 2D-self-potential data, despite their invasive nature.

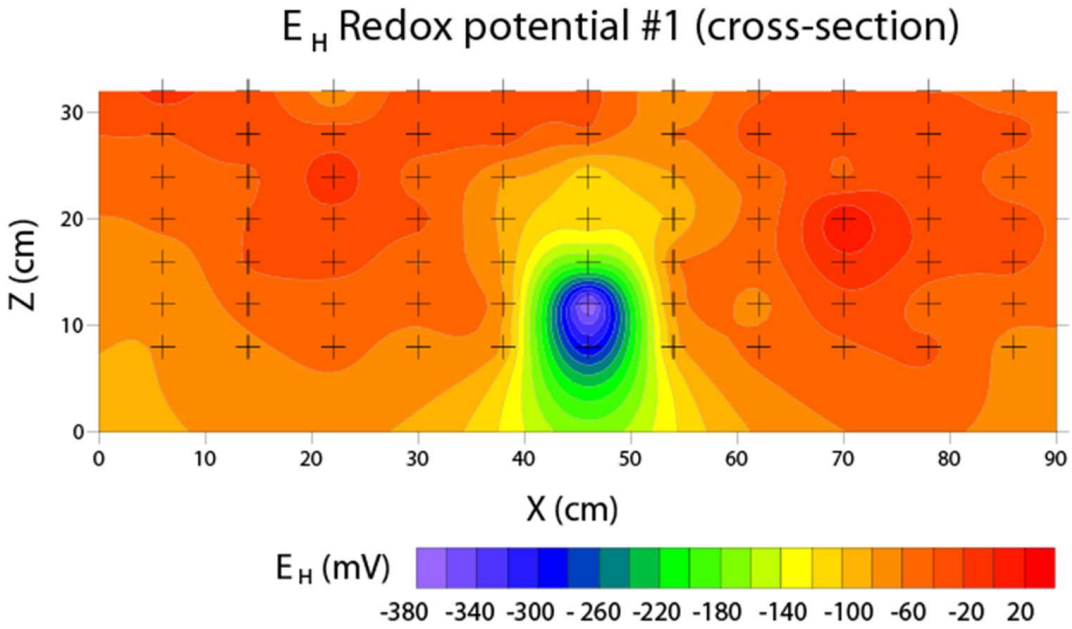

Figure 10. Vertical measurements conducted during measurement set #1, which included only redox potential measurements. This plot shows the EH distribution of the tank in the side view (x/z). Dark blues at the center of the section indicate a strong negative redox potential anomaly at the bottom of the metallic bar, which favors the oxidation of ions such as Fe^{2+} and Fe^{3+}.

Measurement Set #3: First, the 2D-surface self-potential data collected during this period experienced a sharp jump from −22 mV to −32 mV at the center position, which did not occur in any of the other measurement sets along the two vertical cross-sections. In addition, the pH measurements showed an anomaly of low pH (pH = 5.9) at the top of the metallic bar (Figure 12). The self-potential signals along the vertical cross-section showed an anomaly of −40 mV, and redox potential measurements produced an anomaly of −210 mV, similar to those observed in previous data sets, though the self-potential data aew suspect due to the sudden jump in the 2D-self-potential data observed during this measurement set.

Measurement Set #4 shows a strong negative self-potential anomaly (Figure 13). The pH data also demonstrated a large anomaly of high pH (pH = 10.3) throughout the metallic bar (Figure 14). Unlike Measurement Set #3, the 2D-self-potential response during this period was very stable in both magnitude and shape; thus, it is unlikely that our measurements greatly disturbed the signal.

During the course of this experiment, evidence of the presence of a bacterial community began to develop in ways outside of those observed by the methods considered above. The first noted occurrence of visual evidence of bacterial growth occurred near the end of Phase 4, when subsurface sand visible at the glass face near the fluid injection point (x = 0 cm to x = 20 cm, y = 0 cm, z = 0 cm to z = 12 cm) began to take on a dark coloration. At first this was considered to be due to the deposition of ferric minerals from the oxidation reduction reactions associated with the oxidation of iron.

Over the next 60 days through the early stages of Phase 5, this dark coloration began to spread on all four faces of the tank. Figure 15 shows this coloration on the sides of the tank, forming a clear horizon that generally coincided with the current height of the phreatic surface and the lower portion of the capillary fringe, though this horizon was not regular throughout the tank. In the front view face (the x/z face at y = 0 cm), the bacterial growth was the most prominent, with a thick region that extended well into the capillary fringe (z = 15 cm) throughout the face, with a slight decrease in height (z = 10 cm), as x approached 90 cm. A small region near the bottom of the fluid injection pipe remained generally coloration free, likely due to injections of fluid pushing bacterial colonies and

their nutrients away from this region. In the back view (the x/z face at y = 45 cm), the height of the coloration follows a linear gradient, beginning at the height of the phreatic surface, z = 10.5 cm at x = 90 cm, and decreasing gradually to z = 0 cm at x = 0 cm. This pattern could be explained by the small hydraulic gradient pushing nutrients away from the region at x = 0 cm and y = 45 cm.

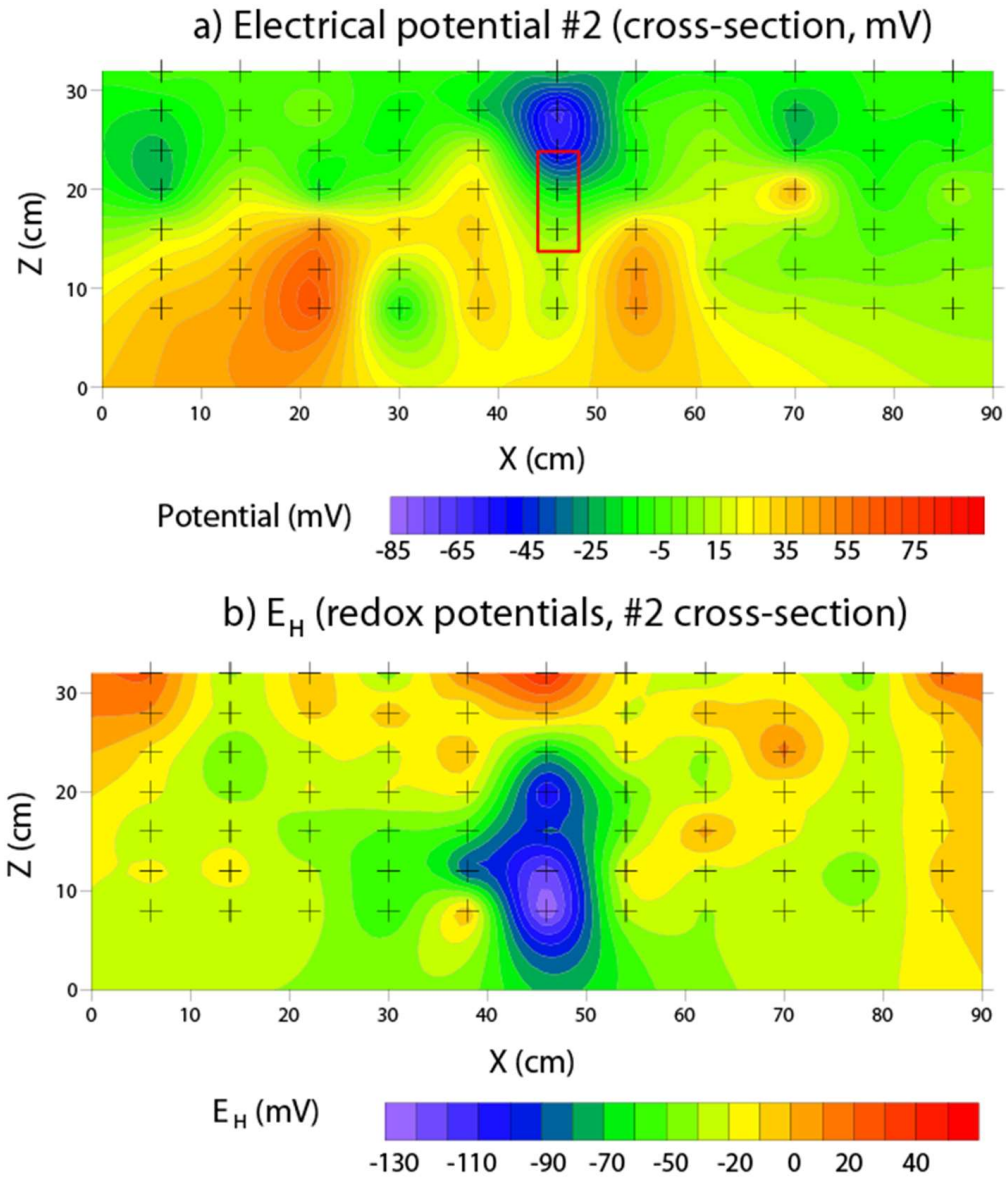

Figure 11. Vertical measurements conducted during measurement set #2, which included redox potential and vertical self-potential measurements. (**a**) The self-potential response along a vertical cross-section of the tank (front view, x/z). Dark blues indicate negative SP potentials, while reds are indicative of positive SP potentials, which show a negative anomaly at the top of the metal bar, though small in magnitude compared to later measurements. (**b**) The EH response of the tank in the front view (x/z). Dark blues at the center of the section indicate a strong negative redox potential anomaly at the bottom of the metallic bar, which favors the oxidation of ions such as Fe^{2+} and Fe^{3+}. This anomaly is not quite as strong in magnitude as in Data Set #1, possibly due to the change in the height of the phreatic surface.

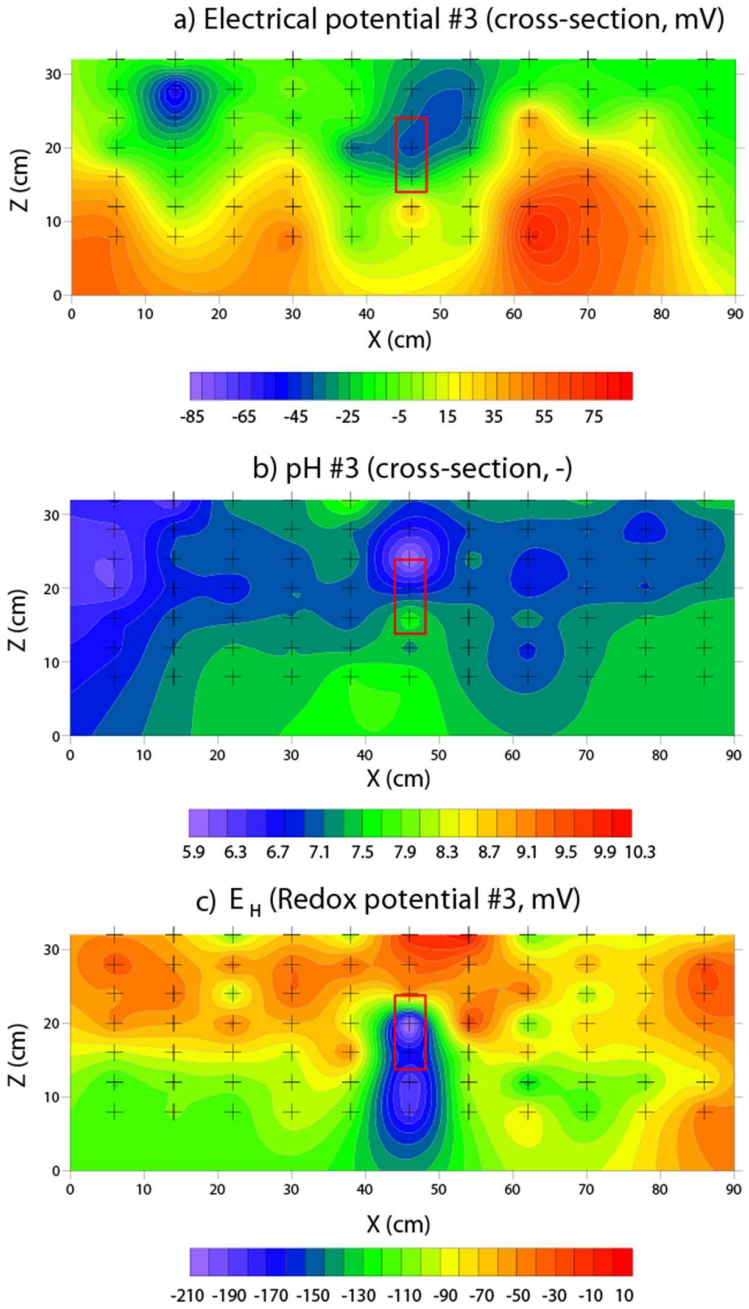

Figure 12. Vertical measurements conducted during measurement set #3, which included redox potential, pH, and self-potential measurements along a vertical cross-section. (**a**) Self-potential response inside the tank along a vertical cross-section (front view, x/z). Dark blues indicate negative SP potentials, while reds are indicative of positive SP potentials, which show a negative anomaly at the top of the metal bar that has become larger in magnitude from previous measurements. (**b**) The pH response of the tank in the front view (x/z). Dark blues and purples indicate low pH values (acidic conditions), while reds and oranges indicate high pH values (basic conditions), and show a slight acidic (low pH) anomaly at the top of the metal bar. (**c**) The EH response of the tank in the front view (x/z). Dark blues at the center of the section indicate a strong negative redox potential anomaly at the bottom of the metallic bar, which favors the oxidation of ions such as Fe^{2+} and Fe^{3+}. This anomaly is slightly larger than that recorded in Measurement Set #2, though not as large as that recorded in Measurement Set #3. The redox half-reaction reduction potential for the couple CO_2/acetate is -290 mV.

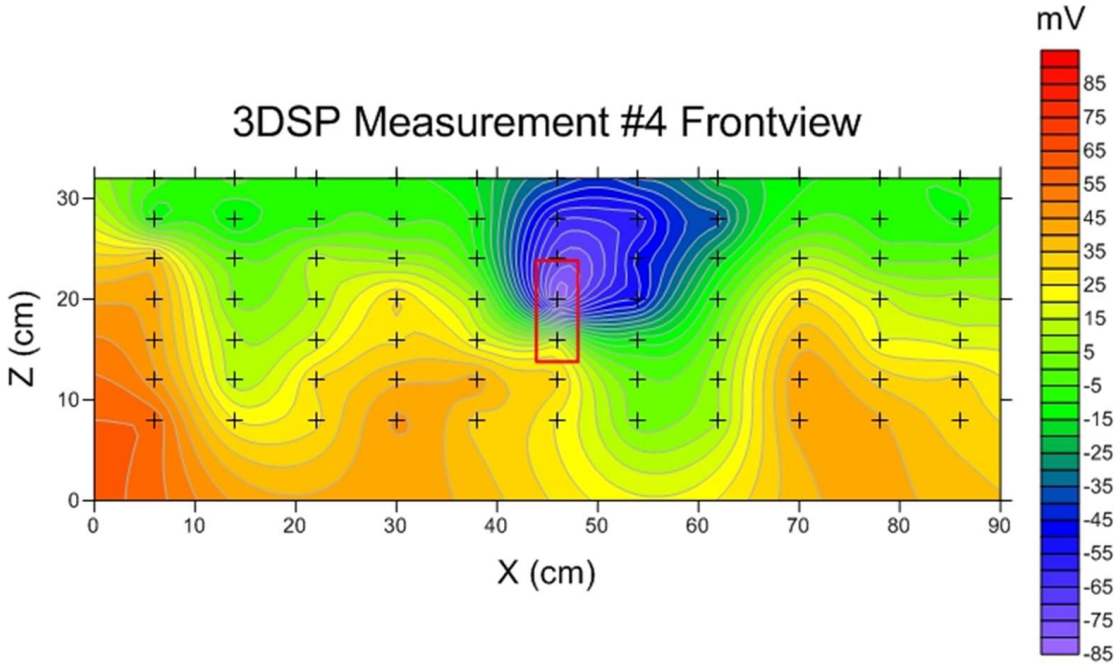

Figure 13. Vertical self-potential measurements conducted during Data Set #4, which included pH and SP measurements along a vertical plane. The vertical self-potential response along a vertical cross-section (x–z plane). The dark blue area corresponds with negative self-potential potentials. The red area is indicative of positive self-potential potentials, which shows the largest positive anomaly.

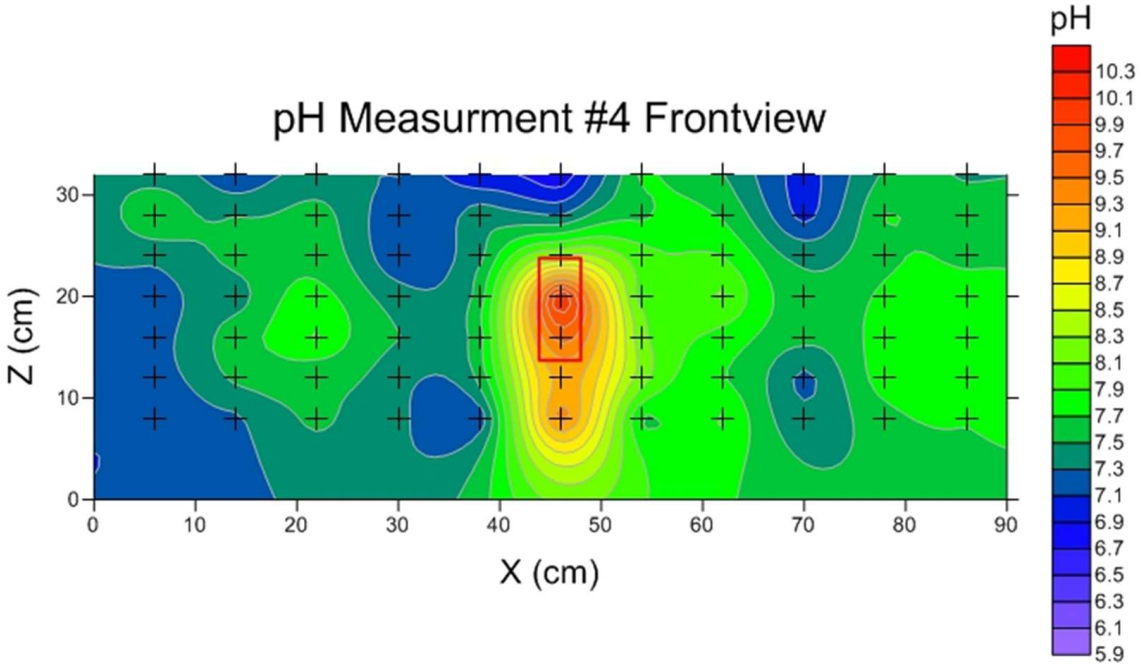

Figure 14. pH distribution along the vertical cross-section. The pH response of the tank in the front view (x/z) for Data Set #4. Dark blues and purples indicate low pH values (acidic conditions), while reds and oranges indicate high pH values (basic conditions). A clean basic anomaly (high pH) is associated with the metallic bar itself. Note the strong gradient in the pH values just above the metallic object. We observe an electrical dipole along the vertical direction.

a) Front view (end of period #5)

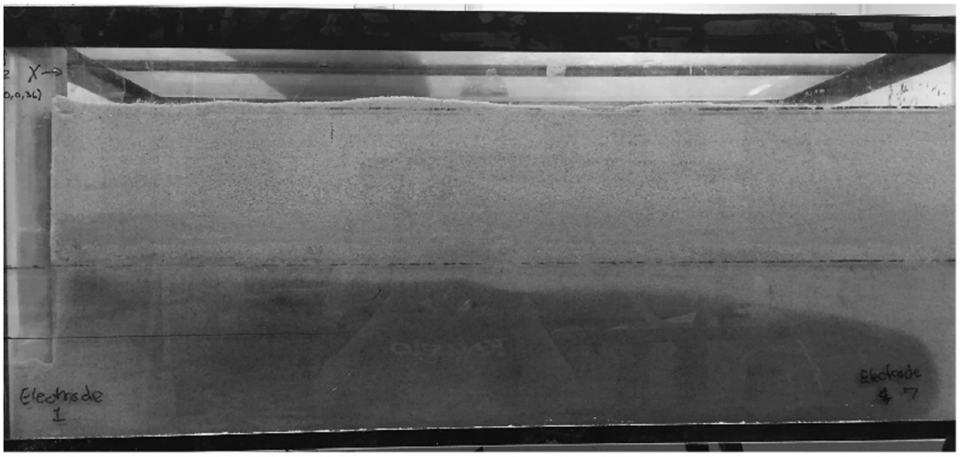

b) Rearview view (end of period #5)

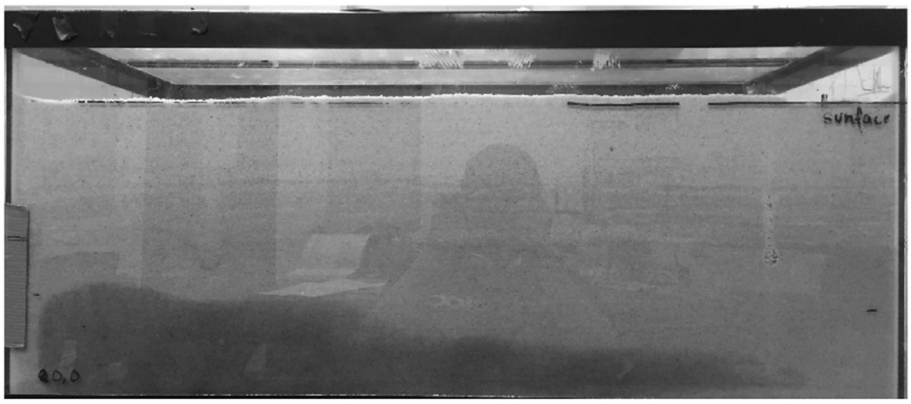

Figure 15. The visible bacterial growth that fully developed within the tank by the end of Phase 5, denoted by the black coloration of the sand below the phreatic surface. (**a**) Front view of the tank (x–z face and y = 0 cm). (**b**) Rearview of the tank (x–z face and y = 45 cm).

This coloration became fully established by Day 182 in the early stages of Phase 5, and persisted unchanged through the end of experimentation. Cores of the tank sediment were extracted for the purpose of sampling the bacterial community; visible colored horizons were observed in several of the cores. Above this horizon, the sand was largely absent of color and odor, even if it contained pore water from the capillary fringe. Below this horizon, the sand was largely black in color and bore a strong sulfurous odor. This color persisted in the cores until they became completely dry, at which point the coloration returned to that of the original sand. This indicates that the coloration was not due to the presence of metallic minerals deposited in the pore space (as a result of the oxidation of iron ions from the metal bar) but was in fact due to a community of bacteria that developed in the tank environment. This was also observed after the end of the experimental phase. Although no measurements were collected during this time and the tank was not regularly monitored, we did observe that the height of this coloration began to drop with the phreatic surface after we ceased maintaining its height.

The DNA/RNA sequencing analysis on the replica experiment indicated that the inoculated acetic acid contains *Acetobacter* spp., an acetobacter-type bacterium. Ferrous iron oxidizing bacteria, *Ferrobacillus* and *Thiobacillus ferrooxidans* and iron-oxidizing bacteria

(*Chlamydobacteriales*, *Gallionella*, *Sphaerotilus*, *Crenothrix*, and *Leptothrix*) were found near the metallic bar. Iron-oxidizing bacteria are acidophilic organisms, taking advantage of the fact that Fe^{2+} is stable at low pH values, whereas above pH 4.5, autooxidation occurs. Iron-oxidizing bacteria are found in long sheaths and belong to the class. The iron-oxidizing bacteria oxidize ferrous ions to a ferric state to obtain their energy; they need oxygen. Iron-oxidizing bacteria colonize the transition zone, where de-oxygenated water from an anaerobic environment flows into an aerobic environment. Under acidic conditions, where ferrous iron is more soluble and stable even in the presence of oxygen, only microbiological processes are responsible for the oxidation of iron, thus making ferrous iron oxidation the major metabolic strategy in iron-rich acidic environments.

4. Discussion

By changing the height of the phreatic surface at the beginning of Phase 1, we were able to significantly reduce the anomaly by placing the majority of the bar within an anaerobic environment. This is because the gradient between the oxidizing environment and the reducing environment, also referred to as the redox gradient, is controlled not only by the location of the water table but also by the thickness of the capillary fringe that forms as a result of capillary action within the pore space of the porous media. At the initial level of the phreatic surface (z = 10.5 cm), the maximum change in this gradient was placed across the center of the metallic bar, and therefore encouraged corrosion processes on the metallic bar itself to occur. When we raised the phreatic surface, the redox gradient shifted accordingly, with the largest gradients no longer placed at the center of the bar, causing the corrosion processes to cease and the 2D-self-potential anomaly to diminish, accordingly.

When we returned the phreatic surface to its original height during Phase 2, we expected that the corrosion processes would start again and a 2D-self-potential anomaly would develop accordingly. However, this did not occur, possibly due to a strong delay time between the change of the water table, the change in height of the capillary fringe, and the slow development of the corrosion processes.

The first injection of the acetic acid solution failed largely because the acetic acid was injected within the water table through the borehole shown in Figure 1 and was not immediately placed in contact with the metallic bar. Our observations demonstrate that any acetic acid that came into contact with the metallic bar by following water into the capillary fringe was not sufficient to facilitate bacterial growth and bolster oxidation-reduction processes to be visible in the self-potential signal. However, the second injection, which was higher in the profile and allowed the acetic acid solution to immediately come into contact with the metallic bar, produced a short-lived, immediate response in the 2D-self-potential anomaly and initiated a gradual response that persisted through the rest of the experiment. This gradual growth was consistent over the course of 50 days, and remained stable afterwards. We believe this represents the development of a bacterial community, as the bacteria began to metabolize the acetate produced by the dissociation of acetic acid after the second application. This is supported by visual evidence of bacterial growth appearing during this time and fully developing during Phase 5 (Figure 15). The bacteria play the role of catalysts in the redox reactions shown in Figure 16.

This anomaly then remained largely stable for the remaining duration of the experiment. A large perturbation occurred following a set of vertical measurements inside the tank that persisted for 18 days during Phase 5. It is unclear why this occurred so dramatically at this particular measurement set and not the other three measurement sets, which were conducted using the same procedure. A possible explanation could be that a small reservoir of acetic acid had been preserved in the center of the metal bar's cylinder, possibly by a small crust of ferrous oxides that had developed within this hollow interior. During the measurements performed inside the tank, this crust was broken by the tool used to excavate the borehole, allowing this acetic acid to enter more saturated regions of the capillary fringe that contained larger populations of bacteria. This could have caused

an increase in the magnitude of the signal that could have lasted for several days until equilibrium conditions were once again reached.

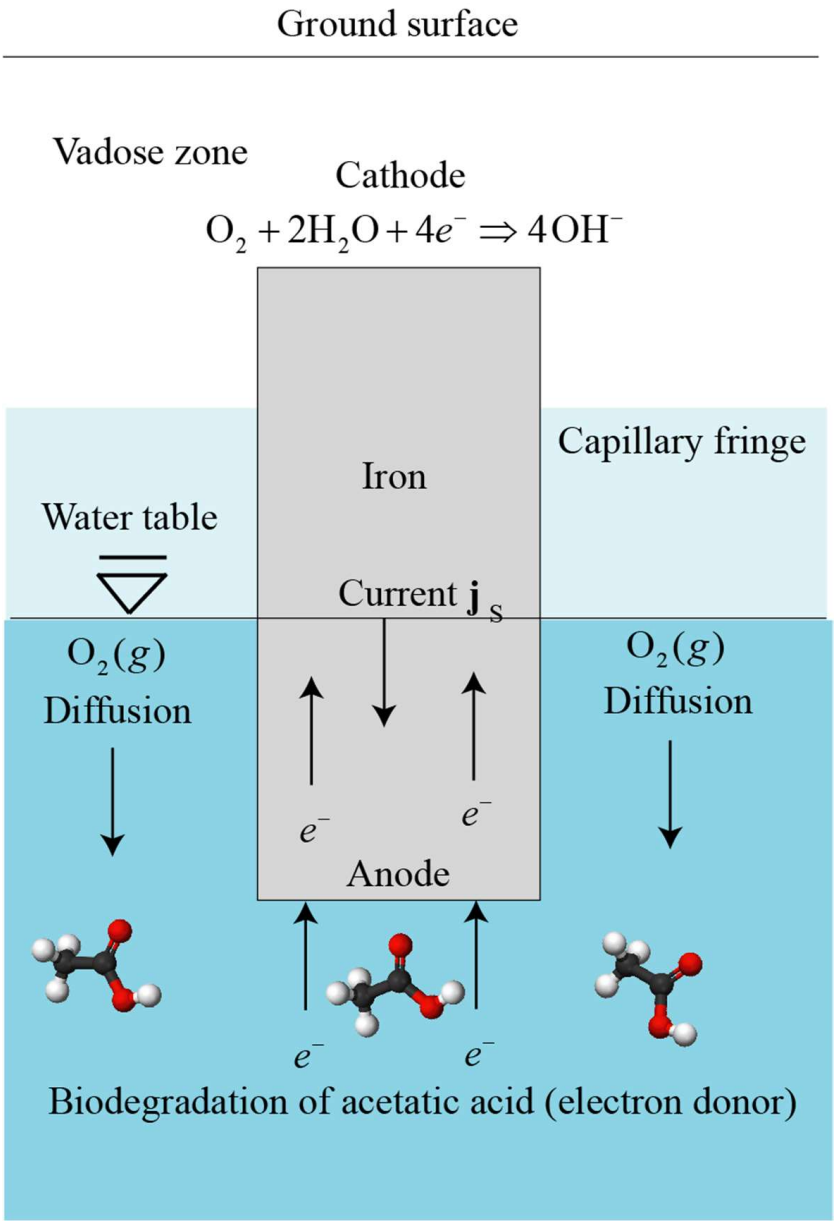

Figure 16. Sketch of the bioelectrochemical cell associated with the buried metallic target in the sandbox. The quantity $\mathbf{j}_S$ denotes the source current density associated with current in the metallic bar. The vadose zone is expected to be rich in oxygen and basic, and the redox potential is expected to be positive, while the area located below the BEC is expected to be oxygen-poor, acidic, and characterized by a negative redox potential. The difference in redox potential between the anode and the cathode drives the current in the BEC.

At the conclusion of the experiment, the anomaly began to decrease, perhaps indicating that the corrosion processes occurring at the metallic bar and all associated processes concerning the acetic acid and bacterial growth were beginning to diminish, perhaps because of the lack of nutrients. However, due to experimentation timelines, the experimentation ended before the anomaly was allowed to diminish to negligible magnitudes.

At Measurement Set #1, the 2D-self-potential anomaly was at the end of Phase 1, which is defined as the phase between perturbations of the phreatic surface. During this time,

a negligible 2D-self-potential anomaly was observed, and from surface measurements it was unclear whether any oxidation-reduction reactions were occurring within the tank. However, the redox potential measurements resulted in the largest of redox potential anomalies observed during experimentation. This indicates that, despite the lack of 2D-self-potential signal, the metal bar was primarily in a location favorable for oxidation, particularly of the Fe and Fe^{2+} ions present within the metal bar. The magnitude of the anomaly relative to later measurements could indicate that the metal bar was primarily in a highly anaerobic environment that favored oxidation and was deprived of free oxygen. In this case, the metal bar would only fall at the lower end of the spatial gradient in the redox potential. Cut off from free oxygen, the oxidation-reduction reactions would cease, and the 2D-self-potential signal would be minimal despite the large redox anomaly observed. It is important to remember that acetic acid was yet to be introduced to the system, so contributions to these measurements from acetate cannot be considered and bacterial mediations of these processes were minimal at best.

In Data Set #2, we had reached Phase 4, where the exponential growth in the 2D-self-potential anomaly had begun to develop following the second injection of acetic acid to the system. Measurement Set #2 took place during the middle of this period and added self-potential and redox potential data inside the tank. A localized negative self-potential anomaly along the vertical plane had formed over the top of the metal bar, being the smallest in spatial extent and comparable to the self-potential measurements of Measurement Set #3 in magnitude. Though the presence and placement of this anomaly was expected, only the sideview data demonstrated a dipolar effect with a small positive pole on the bottom of the metal bar. This could be because the processes responsible for the source current were still developing in association with the growth of bacterial communities (the 2D-self-potential anomaly was only between -16 and -20 mV during these measurements, whereas it remained between -25 mV to -35 mV in Phases 5 and 6). The redox conditions at this stage had dropped significantly, though the anomaly was still present. This could be due to the drop in the phreatic surface placing the bar more in the center of the spatial gradient of the redox potential, which would cause the bottom of the bar to be at a less negative area of this gradient.

Data Set #3 produced the most interesting results. First, the redox potentials increased slightly, possibly due to the larger community of bacteria providing a higher concentration of electrons to be donated to an oxidant. We also saw a self-potential anomaly inside the tank, consistent with those observed in previous data sets, though the results are suspect due to the following discussion. This measurement set is characterized by a large jump in the 2D-self-potential data between Day 158 and Day 159, the two days over which Measurement Set #3 occurred. It is worth noting that the measurements at Station 28, the center point above the metal bar, were conducted on Day 158, while later measurements, such as the side view measurements, were conducted on Day 159. We also noted that, unlike previous measurement sets, it was difficult to excavate a borehole at Station 28 in order to allow a probe contact with the system at the desired depth. This hole was intended to go through the center of the metal bar through its hollow interior. We determined that this difficulty was due to the presence of ferrous oxides that had formed a crust in the center of the metallic bar, cementing the sediment and filling the pore space. This could have trapped a small concentration of acetic acid from the second injection some 90 days prior, where it was injected at a depth of $z = 27$ cm at the top of the metal bar. Though it is unknown how quickly the acetic acid would infiltrate into the system, perhaps a small concentration became trapped within this ferrous oxide crust between Measurement Set #2 and #3. By creating a borehole through this crust, we then forced this acetic acid to enter more anaerobic regions of the metal bar, where it dissociated into hydrogen ions and acetate and fueled a small bloom in the bacterial community. This claim is supported by the pH measurements, where a localized anomaly of relatively low pH (pH = 5.9) was observed at the top of the metal bar. We would suspect that there would be a region of high pH at the top of the metallic bar due to the production of OH^- ions from the reduction of

O_2 at the end of the oxidation-reduction sequences. However, the opposite was observed. This could perhaps be due to the presence of acetic acid increasing the pH of this region through the production of H^+ ions through its dissociation, prior to this measurement set $CH_3 - CO_2H \Rightarrow CH_3 - CO_2{}^- + H^+$. The oxidation of acetate in the presence of Fe(III) can be written as

$$CH_3 - CO_2{}^- + 8Fe^{3+} + 4H_2O \Rightarrow 2HCO_2{}^- + 8Fe^{2+} + 9H^+ + O_2 \quad (11)$$

and does not require oxygen to occur. Furthermore, this reaction can be promoted by bacteria [32]. This is also at the opposite of the following oxidation reaction

$$CH_3 - CO_2{}^- + H^+ + 2O_2 \Rightarrow 2CO_2 + 2H_2O \quad (12)$$

At the cathode, the half-reactions can be written as,

$$O_2 + 4H^+ + 4e^- \Rightarrow 2H_2O \quad (13)$$

$$4Fe^{2+} + O_2 + 4H^+ \Rightarrow 4Fe^{3+} + 2H_2O \quad (14)$$

$$Fe^{3+} + 3H_2O \Rightarrow Fe(OH)_3 + 3H^+ \quad (15)$$

The self-potential and redox potential anomalies observed in this measurement set, however, appeared to be consistent with our expectations, with a large negative redox potential anomaly focused on the bottom of the metal and a large negative self-potential anomaly focused on the top of the metal bar [3,7]. Equation (14) is known to be promoted by iron oxidizer bacteria such as *Acidithiobacillus ferrooxidans* [33].

Our last set of measurements, Data Set #4, produced a strong negative self-potential anomaly inside the tank just above the metallic bar: the largest observed during measurement. It also demonstrated the clearest dipolar anomaly in the self-potential data, with a positive pole visible at the bottom of the metallic bar, which matches our expectations of the current density produced due to series of oxidation-reduction reactions within the tank. We also observed a high pH anomaly, with a region of pH= 8–10 observed throughout the length of the metallic bar. This is consistent with the pH anomaly observed by Rittgers et al. (2013) [3] and coincides with the production of hydroxide ions, the final product of the aerobic redox reactions associated with both the oxidation of Fe^{2+} and Fe^{3+} and the oxidation of acetate by aerobic bacteria.

The lack of a low pH anomaly at this timestep could also demonstrate that acetic acid originally injected at the beginnings of Phase 3 and Phase 4 has either become extremely diluted throughout the tank or has fully dissociated into acetate and hasbeen removed from the system through microbial processes. This could explain the drop in the magnitude of the 2D-self-potential anomaly at the end of Phase 6 before the end of experimentation, as the acetate that bacteria (both aerobic and anaerobic) oxidize as part of their metabolization would have disappeared, therefore causing the bacterial community to cease their activity.

These measurements provide us with additional observations to supplement and explain the signal observed in the 2D-self-potential anomaly. The extremely negative redox potentials observed during Measurement Set #1 confirms that the metal bar was primarily in an environment that favored only the reduction of Fe^{2+} and Fe^{3+}, which prevented oxidation-reduction reactions by placing the conductive pathway entirely within an oxygen poor environment, and therefore providing few electron acceptors to complete the reaction. This resulted in a low 2D-self-potential response at the surface, which maintained itself throughout Phases 1, 2, and 3. In Measurement Set #2 and Phase 4, the reduction in the redox potential shows that the bar was now placed higher in the redox gradient, and now had access to an anoxic environment at the top of the bar, thus allowing for the

redevelopment of the 2D-self-potential signal. This persisted through Measurement Set #3 and Phase 5.

The small vertical self-potential response recorded during Measurement Set #2 corresponds with the redevelopment of the 2D-self-potential signal during Phase 4. This vertical self-potential signal grew over time in Measurement set #3 and #4 to correspond with the growth of 2D-self-potential signal in Phase 5 and 6, respectively. The vertical distribution of the self-potential signals also reflects the asymmetrical behavior observed in the (surface) 2D-self-potential signals, which suggests that at least some of the chemical processes producing the source currents observed in the self-potential method are spatially separated from the bar itself, which could be controlled by a slight gradient in the hydraulic head pushing aqueous Fe^{2+}, Fe^{3+}, ferrous oxides, and acetate in the positive x and y directions. These components could then connect to the conductive body of the metal bar through a network of bacteria, who communicate electrons between one another and between particles of ferrous oxides with microfilaments.

As discussed above, the two pH measurement sets demonstrate that something acidic, likely the acetic acid injected into the tank at Phases 3 and 4, was still present in the system during Phase 5 and Measurement Set #3, and likely was responsible for the brief spike in the 2D-self-potential data observed in Phase 5 after being disturbed by the invasive nature of the measurements along a vertical cross-section. This was not observed in Measurement Set #4, with the low pH anomaly being replaced with a high pH anomaly consistent with previous studies. This indicates that acetate from the dissociation of acetic acid had been nearly fully consumed, which would then cause the 2D-self-potential signal to diminish should the experiment have been continued. The 2D-self-potential anomaly likely sustained itself for this long because acetic acid, being a weak acid, does not fully dissociate when in solution. Therefore, acetate would then be produced slowly as bacteria consumed the available acetate and then allowed further dissociation to occur to return the system to equilibrium conditions.

5. Conclusions

A sandbox experiment was conducted over a period of 327 days by monitoring self-potential signals associated with the corrosion of a metallic object taken as a proxy of an ore body and placed through the capillary fringe. The use of self-potential measurements performed at the air-open top of the sandbox can be used to monitor the redox activity at the surface of the ore body. The redox reactions are likely mediated by bacterial communities present in the sandbox. The presence of bacteria was responsible for a visible change of the color of the sand at the end of the period of exponential growth of the self-potential anomaly. The metallic object plays the role of a (bio-)geobattery at the location of the capillary fringe and can encourage the growth of bacterial communities in the presence of an organic contaminant by providing a conductive pathway between regions containing high concentrations of oxidants and regions containing high concentrations of reductants that are spatially separated by the capillary fringe. This allows metabolization processes of aerobic bacterium to continue in regions where free oxygen is limited due to diffusion gradients by providing a conductive pathway to regions rich in free oxygen across the redox gradient. The self-potential anomaly associated with the corrosion processes of the metal bar appear to be correlated with the height of the phreatic surface relative to the location of the metallic bar. This was observed in the first phase of the experiment, where an increase in the height of the phreatic surface produced an immediate decrease in the magnitude of the self-potential anomaly. This work underlines how self-potential signals can be used to locate ore bodies and to monitor redox processes present at their surface, especially when redox processes are mediated by bacterial activity such as, for instance, in bioleaching.

Author Contributions: The authors contributed equally to the paper. All authors have read and agreed to the published version of the manuscript.

Funding: This research received no external funding.

Data Availability Statement: All the data used to generate the figures can be obtained from the corresponding author Zhaoyang Su (2019310419@student.cup.edu.cn) and André Revil (andre.revil@univ-smb.fr).

Acknowledgments: A. Revil thanks the CNRS for its support over the years. Z. Su is funded by the China Scholarship Council (202106440109).

Conflicts of Interest: The author declares no conflict of interest.

References

1. Sato, M.; Mooney, H.M. The electrochemical mechanism of sulfide self-potentials. *Geophysics* **1960**, *25*, 226–249. [CrossRef]
2. Castermant, J.; Mendonça, C.A.; Revil, A.; Trolard, F.; Bourrié, G.; Linde, N. Redox potential distribution inferred from self-potential measurements associated with the corrosion of a burden metallic body. *Geophys. Prospect.* **2008**, *56*, 269–282. [CrossRef]
3. Rittgers, J.B.; Revil, A.; Karaoulis, M.; Mooney, M.A.; Slater, L.D.; Atekwana, E.A. Self-potential signals generated by the corrosion of buried metallic objects with application to contaminant plumes. *Geophysics* **2013**, *78*, EN65–EN82. [CrossRef]
4. Constable, S.; Kowalczyk, P.; Bloomer, S. Measuring marine self-potential using an autonomous underwater vehicle. *Geophys. J. Int.* **2018**, *215*, 49–60. [CrossRef]
5. Bigalke, J.; Grabner, E.W. The geobattery model: A contribution to large scale electrochemistry. *Electrochim. Acta.* **1997**, *42*, 3443–3452. [CrossRef]
6. Timm, F.; Möller, P. The relation between electric and redox potential: Evidence from laboratory and field measurements. *J. Geochem. Explor.* **2001**, *72*, 115–128. [CrossRef]
7. Maineult, A. Estimation of the electrical potential distribution along metallic casing from surface self-potential profile. *J. Appl. Geophys.* **2016**, *129*, 66–78. [CrossRef]
8. Revil, A.; Fernandez, P.; Mao, D.; French, H.K.; Bloem, E.; Binley, A. Self-potential monitoring of the enhanced biodegradation of an organic contaminant using a bioelectrochemical cell. *Lead. Edge* **2015**, *34*, 198–202. [CrossRef]
9. Kawada, Y.; Kasaya, T. Marine self-potential survey for exploring seafloor hydrothermal ore deposits. *Sci. Rep.* **2017**, *7*, 1–12. [CrossRef]
10. Kawada, Y.; Kasaya, T. Self-potential mapping using an autonomous underwater vehicle for the Sunrise deposit, Izu-Ogasawara arc, southern Japan. *Earth Planets Space* **2018**, *70*, 142. [CrossRef]
11. Revil, A.; Ehouarne, L.; Thyreault, E. Tomography of self-potential anomalies of electrochemical nature. *Geophys. Res. Lett.* **2001**, *28*, 4363–4366. [CrossRef]
12. Mendonça, C.A. Forward and inverse self-potential modeling in mineral exploration. *Geophysics* **2007**, *73*, F33–F43. [CrossRef]
13. Su, Z.; Tao, C.; Shen, J.; Revil, A.; Zhu, Z.; Deng, X.; Nie, Z.; Li, Q.; Liu, L.; Wu, T. 3D self-potential tomography of seafloor massive sulfide deposits using an autonomous underwater vehicle. *Geophysics* **2022**, *87*, B255–B267. [CrossRef]
14. Su, Z.; Tao, C.; Zhu, Z.; Revil, A.; Shen, J.; Nie, Z.; Li, Q.; Deng, X.; Zhou, J.; Liu, L. Joint interpretation of marine self-potential and transient electromagnetic survey for seafloor massive sulfide (SMS) deposits: Application at TAG hydrothermal mound, mid-Atlantic ridge. *J. Geophys. Res. Solid Earth* **2022**, *127*, e2022JB024496. [CrossRef]
15. Zhu, Z.; Tao, C.; Shen, J.; Revil, A.; Deng, X.; Liao, S.; Zhou, J.; Wang, W.; Nie, Z.; Yu, J. Self-potential tomography of a deep-sea polymetallic sulfide deposit on Southwest Indian Ridge. *J. Geophys. Res. Solid Earth* **2020**, *125*, e2020JB019738. [CrossRef]
16. Zhu, Z.; Shen, J.; Tao, C.; Deng, X.; Wu, T.; Nie, Z.; Wang, W.; Su, Z. Autonomous-underwater-vehicle-based marine multicomponent self-potential method: Observation scheme and navigational correction. *Geosci. Instrum. Methods Data Syst.* **2021**, *10*, 35–43. [CrossRef]
17. Eppelbaum, L.V. Review of processing and interpretation of self-potential anomalies: Transfer of methodologies developed in magnetic prospecting. *Geosciences* **2021**, *11*, 194. [CrossRef]
18. Minsley, B.J.; Sogade, J.; Morgan, F.D. Three-dimensional self-potential inversion for subsurface DNAPL contaminant detection at the Savannah River Site, South Carolina. *WRR* **2007**, *43*, W04429. [CrossRef]
19. Abdelrahman, E.M.; Essa, K.S.; Abo-Ezz, E.R.; Soliman, K.S. Self-potential data interpretation using standard deviations of depths computed from moving-average residual anomalies. *Geophys. Prospect.* **2006**, *54*, 409–423. [CrossRef]
20. Abdelrahman, E.M.; Saber, H.S.; Essa, K.S.; Fouda, M.A. A least-squares approach to depth determination from numerical horizontal self-potential gradients. *Pure Appl. Geophys.* **2004**, *161*, 399–411. [CrossRef]
21. Essa, K.S.; Diab, Z.E.; Mehanee, S.A. Self-potential data inversion utilizing the Bat optimizing algorithm (BOA) with various application cases. *Acta Geophys.* **2023**, *71*, 567–586. [CrossRef]
22. Ballester, A.; González, F.; Blázquez, M.; Gómez, C.; Mier, J. The use of catalytic ions in bioleaching. *Hydrometallurgy* **1992**, *29*, 145–160. [CrossRef]
23. Vera, M.; Schippers, A.; Hedrich, S.; Sand, W. Progress in bioleaching: Fundamentals and mechanisms of microbial metal sulfide oxidation—Part A. *Appl. Microbiol. Biotechnol.* **2022**, *106*, 6933–6952. [CrossRef]

24. Ogram, A.; Sayler, G.S.; Barkay, T. The extraction and purification of microbial DNA from sediments. *J. Microbiol. Methods* **1987**, *7*, 57–66. [CrossRef]
25. Lever, M.A.; Torti, A.; Eickenbusch, P.; Michaud, A.B.; Šantl-Temkiv, T.; Jørgensen, B.B. A modular method for the extraction of DNA and RNA, and the separation of DNA pools from diverse environmental sample types. *Front. Microbiol.* **2015**, *6*, 476. [CrossRef] [PubMed]
26. Revil, A.; Finizola, A.; Gresse, M. Self-potential as a tool to assess groundwater flow in hydrothermal systems: A review. *J. Volcanol. Geotherm. Res.* **2023**, *437*, 107788. [CrossRef]
27. Tikhonov, A.N.; Arsenin, V.Y. *Solutions of Ill-Posed Problems*; John Wiley & Sons: Hoboken, NJ, USA, 1977.
28. Michael, Z.; Ekaterina, T. Minimum support nonlinear parametrization in the solution of a 3D magnetotelluric inverse problem. *Inverse. Probl.* **2004**, *20*, 937.
29. Jardani, A.; Revil, A.; Bolève, A.; Dupont, J.P. Three-dimensional inversion of self-potential data used to constrain the pattern of groundwater flow in geothermal fields. *J. Geophys. Res. Solid Earth* **2008**, *113*, B09204. [CrossRef]
30. Revil, A.; Jardani, A. *The Self-Potential Method: Theory and Applications in Environmental Geosciences*; Cambridge University Press: Cambridge, UK, 2013.
31. Mao, D.; Revil, A. Induced polarization response of porous media with metallic particles—Part 3: A new approach to time-domain induced polarization tomography. *Geophysics* **2016**, *81*, D345–D357. [CrossRef]
32. Hattori, S.; Galushko, A.S.; Kamagata, Y.; Schink, B. Operation of the CO dehydrogenase/acetyl coenzyme A pathway in both acetate oxidation and acetate formation by the syntrophically acetate-oxidizing bacterium *Thermacetogenium phaeum* . *J. Bacteriol.* **2005**, *187*, 3471–3476. [CrossRef]
33. Valdés, J.; Pedroso, I.; Quatrini, R.; Dodson, R.J.; Tettelin, H.; Blake, R.; Eisen, J.A.; Holmes, D.S. *Acidithiobacillus ferrooxidans* metabolism: From genome sequence to industrial applications. *BMC Genom.* **2008**, *9*, 1–24. [CrossRef] [PubMed]